

An Atomistic Fingerprint Algorithm for Learning *Ab Initio* Molecular Force Fields

Yu-Hang Tang , Dongkun Zhang , and George Em Karniadakis

Division of Applied Mathematics, Brown University, Rhode Island, USA 02912

Abstract Molecular fingerprints, i.e. feature vectors describing atomistic neighborhood configurations, is an important abstraction and a key ingredient for data-driven modeling of molecular energy and inter-atomic force. In this paper, we present the Density-Encoded Canonically Aligned Fingerprint (DECAF) fingerprint algorithm, which is robust and efficient, for fitting per-atom scalar and vector quantities. The fingerprint is essentially a continuous density field formed through the superimposition of smoothing kernels centered on the atoms. We propose that the ‘distance’ between the fingerprints be measured as a weighted L_2 norm of their difference. Rotational invariance of the fingerprint is achieved by aligning, for each fingerprint instance, the neighboring atoms onto a set of local canonical coordinate frame computed from a kernel minisum optimization procedure. We show that this approach is superior over PCA-based methods especially when the atomistic neighborhood is sparse and/or contains symmetry. To minimize the computational cost, we derive numerical recipes for discrete sampling and evaluation of the fingerprint using optimal quadrature rules. We also experiment on the choice of weight functions for constructing the density fields, and characterize their performance for fitting interatomic potentials. The applicability of the fingerprint is demonstrated through a set of realistic benchmark problems.

Keywords: active learning, Gaussian process, quantum mechanics, molecular dynamics, next generation force fields

1 Introduction

Molecular Dynamics (MD) simulations have been widely used for studying atomistic systems, *e.g.* proteins and catalysts, due to their ability to precisely capture transient events and to predict macroscopic properties from microscopic details [1,2]. In its most prevalent implementation, the trajectory of an atomistic system is integrated in time according to the Newton’s law of motion using forces calculated as the negative gradient of a Hamiltonian, whose functional form and parameters are collectively referred to as a force field [3–5]. Traditionally, the pairwise and many-body terms that comprise a force field are derived by fitting to quantum mechanical calculations and experimental data.

Three properties directly relate to the applicability of a force field: accuracy, transferrability, and complexity [6,7]. Over the years, a large number of force fields have been developed, each carrying

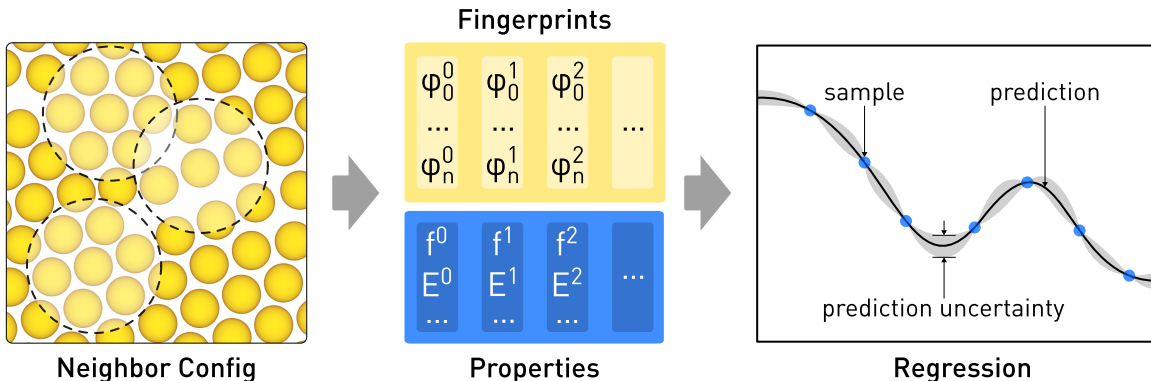


Figure 1: In the pipeline of machine learning-driven molecular computations, atomistic neighborhood configurations are transformed into feature vectors, called fingerprints, and used to train non-linear regression models.

a particular emphasis over these three properties. However, the combinatorial complexity of atomistic systems can easily outpace force field development efforts, the difficulty of which explodes following the curse of dimensionality [8]. A deceptively simple system that can demonstrate the situation is water, a triatomic molecule with a well-characterized molecular structure. In fact, all common water models, such as SPC-E, TIP3P, and TIP4P, have only succeeded in reproducing a small number of structural and dynamical properties of water due to the difficulty in modeling strong intermolecular many-body effects such as hydrogen bonding and polarization [9,10].

In lieu of a force field, quantum mechanical (QM) calculations can be employed straightforwardly to drive molecular dynamics simulations. The method achieves significantly better accuracy and transferability by solving for the electronic structure of the system. However, the computational complexity of QM methods is at least cubic in the number of electrons, and consequently the time and length scales accessible by QM-driven molecular dynamics are severely constrained.

Assuming that there is smoothness in the potential energy surface of the atomistic system, one possible strategy to accelerate QM-driven molecular dynamics is to use QM calculations on only a subset of the time steps, and to interpolate for similar atomic configurations [11–14]. A schematic overview of the process is given in Figure 1, which is enabled by the recent development of high-dimensional nonlinear statistical learning and regression techniques such as Gaussian process regression (GPR) [15] and artificial neural networks [16].

This paper focuses on a particular aspect of the machine-learning-driven molecular computation pipeline, *i.e.* fingerprint algorithms, whose importance arises naturally from the aforementioned regression protocol. A fingerprint is an encoding of an atomistic configuration that can facilitate regression tasks such as similarity comparison across structures consisting of variable numbers of atoms and elements. As has been pointed out previously [12], a good fingerprint should possess the following properties:

1. It can be encoded as a fixed-length vector so as to facilitate regression (particularly for artificial neural networks).
2. It is *complete*, *i.e.* different atomistic neighborhood configurations lead to different fingerprints

and vice versa, and the difference between the fingerprints should be proportional to the intrinsic difference between the atomistic neighborhood configurations.

3. It is *continuous* with regard to atomistic coordinates, and the change in fingerprint should be approximately proportional to the structural variation as characterized by, for example, some internal coordinates.
4. It is *invariant* under permutation, rotation, and translation.
5. It is computationally feasible and straightforward to implement.

Before we proceed to the details of our work, we will first briefly review several fingerprints that are closely related to our work, *i.e.* the Smooth Overlap of Atomic Positions (SOAP) kernel [12], the Coulomb matrix [17], and the Graph Approximated Energy (GRAPE) kernel [18].

Smooth Overlap of Atomic Positions (SOAP): The SOAP kernel is built on the idea of representing atomistic neighborhoods as smoothed density fields using Gaussian kernels each centered at a neighbor atom. Similarity is measured as the inner product between density fields, while rotational invariance is achieved by integrating over all possible 3D rotations, which can be performed analytically using the power spectrum of the density field. In fact, our fingerprint algorithm is inspired by this idea of treating atoms as smoothed density fields. However, we take a different approach to endorse the fingerprint with rotational invariance, and use the Euclidean distance instead of inner product as a distance metric.

Coulomb Matrix: The practice of using graphs to represent atomistic neighbor configurations was first implied by the Coulomb matrix, and later further formulated in the GRAPE kernel, where the *diffusion distance* was proposed as a similarity measure between different local chemical environments [19]. The idea is to construct an undirected, unlabeled graph $G = (V, E)$ with atoms acting as the vertices and pairwise interactions setting the weights of the edges. For example, the Coulomb matrix can be treated as a physically-inspired Laplacian matrix [20]

$$\mathbf{M} = \mathbf{D} - \mathbf{A} \quad (1)$$

$$\mathbf{D}_{IJ} = \begin{cases} 0.5 Z_I^{2.4} & \text{if } I = J \\ 0 & \text{if } I \neq J \end{cases} \quad (2)$$

$$\mathbf{A}_{IJ} = \begin{cases} 0 & \text{if } I = J \\ \frac{Z_I Z_J}{\|\mathbf{R}_I - \mathbf{R}_J\|} & \text{if } I \neq J \end{cases} \quad (3)$$

where the degree matrix \mathbf{D} encodes a polynomial fit of atomic energies to the nuclear charge, while the adjacency matrix \mathbf{A} corresponds to the Coulombic interactions between all pairs of atoms. Due to the use of only relative positions between atoms in the adjacency matrix, the Coulomb matrix is automatically invariant under translation and rotation. However, the matrix itself is not invariant under permutation, as swapping the order of two atoms will result in an exchange of the corresponding columns and the rows. To address this, the sorted list of eigenvalues of the Coulomb matrix can be used instead as a feature vector, while an L^p norm can be used as a distance metric. In practice, due to the fact that the number of

neighbor atoms may change, the shorter list is padded with zero in a distance computation.

Graph Approximated Energy (GRAPE): The GRAPE kernel evaluates the simultaneous random walks on the direct product of the two graphs representing two atomistic neighborhood configurations. Permutational invariance is achieved by choosing a uniform starting and stopping distribution across nodes of both graphs. However, the cost of distance computation between two graphs scales as $O(N^2)$ with a one-time per-graph diagonalization cost of $O(N^3)$.

In the sections below, we present our new fingerprint algorithm, namely the Density-Encoded Canonically Aligned Fingerprint (DECAF). The paper is organized as follows: in Section 2, we introduce a robust algorithm that can determine canonical coordinate frames for obtaining symmetry-invariant projections; in Section 3, we present numerical recipes to use smoothed atomistic density fields as a fingerprint for molecular configuration; in Section 4, we demonstrate the capability of the fingerprint via examples involving the regression of atomistic potential energy surfaces; in Section 5, we discuss the connection between our algorithm and previously proposed ones; we conclude with a discussion in Section 6.

2 Localized Canonical Coordinate Frame for Rotationally Invariant Description of Atomistic Neighborhood

2.1 Kernel Minisum Approach

To improve model generalization while minimizing data redundancy, a fingerprint algorithm should be able to recognize atomistic structures that differ only by a permutation of atoms within the same element or a rigid-body transformation, and extract feature vectors invariant under these transformations. As summarized in Table 1, a variety of strategies have been successfully employed by common fingerprint algorithms to achieve rotational invariance.

However, these approaches do not provide a means for the acquisition of vector-valued quantities in a rotational invariant form. One approach is to only acquire and interpolate the potential energy, a scalar quantity, and then take the derivative of the energy interpolation. This approach, however, further triggers the need for methods to decompose the total energy among the atoms because it is a property of the entire system rather than individual atoms [21].

Another approach proposed by Li *et al.* [13, 22] is to project vector quantities onto a potentially overcomplete set of non-orthogonal basis vectors obtained from a weighted sum of the atomic coordinate vectors:

$$\mathbf{v}_k = \sum_i \mathbf{x}_i \exp \left[- \left(\frac{\|\mathbf{x}_i\|}{R_c} \right)^{p_k} \right]. \quad (4)$$

However, the approach may suffer from robustness issues. For example, all of the \mathbf{v}_k generated with different p_k will coincide if the radial distance of the atoms are all equal. As a second example, the

configuration with 4 atoms at $(r \cos \varepsilon, r \sin \varepsilon), (0, r), (-r, 0), (0, -r)$ yields

$$\mathbf{V}_k = c \cdot [(r \cos \varepsilon, r \sin \varepsilon) + (0, r) + (-r, 0) + (0, -r)] \quad (5)$$

$$= c \cdot r \cdot (1 - \cos \varepsilon, \sin \varepsilon). \quad (6)$$

Thus, if ε gets close to zero, \mathbf{V}_k will always point toward either $(0, 1)$ or $(0, -1)$, even if the vector quantity of interest may point in other directions.

Table 1: Comparison of strategies used by fingerprint algorithms to obtain feature vectors which are invariant under translation, permutation, and rotation.

Fingerprint	Invariance		
	Translation	Permutation	Rotation
Coulomb matrix [17]	relative distance	sorting eigenvalues	all vs. all graph
Behler [11]	relative distance	summation	ignoring angular information
SOAP [12]	relative distance	summation	integrating over all rotations
GRAPE [18]	relative distance	uniform distribution	uniform distribution

Here, we present a robust kernel PCA-inspired algorithm for the explicit determination of a canonical coordinate frame, within which the projection of the atomistic neighborhood is invariant under rigid-body rotation. Furthermore, the canonical coordinate frame can be directly used to capture vector-valued quantities in a rotational-invariant form. Given N atoms with position $\mathbf{x}_1, \dots, \mathbf{x}_N \in \mathbb{R}^d$, we first formulate the L_p PCA algorithm as an optimization problem where we seek a unit vector \mathbf{w}^* that maximizes the sum of projection of the data:

$$\mathbf{w}^* = \operatorname{argmax}_{\|\mathbf{w}\|=1} \sum_{i=1}^N |\mathbf{w}^\top \mathbf{x}_i|^p \quad (7)$$

$$= \operatorname{argmax}_{\|\mathbf{w}\|=1} \sum_{i=1}^N |r_i|^p |\mathbf{w}^\top \mathbf{e}_i|^p, \quad (8)$$

where $r_i = \|\mathbf{x}_i\|$ is the distance from the origin to atom i , $\mathbf{e}_i = \mathbf{x}_i/r_i$ is the unit vector pointing toward atom i , respectively. The optimization process can only uniquely determine the orientation of a projection vector up to a line, because $|\mathbf{w}^\top \mathbf{e}| \equiv |-\mathbf{w}^\top \mathbf{e}|$. As a consequence, further heuristics are needed to identify a specific direction for the PCA vectors.

To overcome this difficulty, we generalize the $|r_i|^p$ term into a weight function $g(r_i)$ and the $|\mathbf{w}^\top \mathbf{e}_i|^p$ term into a bivariate kernel function $\kappa(\mathbf{w}, \mathbf{e}_i)$. We then attempt to seek a unit vector \mathbf{w}^* that minimizes the kernel summation:

$$\mathbf{w}^* = \operatorname{argmin}_{\|\mathbf{w}\|=1} \sum_{i=1}^N g(r_i) \kappa(\mathbf{w}, \mathbf{e}_i). \quad (9)$$

In particular, we have found a square angle (SA) kernel and an exponentiated cosine (EC) kernel as

two robust options:

$$\kappa_{\text{SA}}(\mathbf{w}, \mathbf{e}) \doteq \frac{1}{2} \arccos^2(\mathbf{w}^\top \mathbf{e}), \quad (10)$$

$$\kappa_{\text{EC}}(\mathbf{w}, \mathbf{e}) \doteq \exp(-\mathbf{w}^\top \mathbf{e}). \quad (11)$$

As shown in Figure 2, both kernels are minimal when \mathbf{w} and \mathbf{e} are parallel, and monotonically reach maximum when the two vectors are antiparallel. Intuitively, optimizing the minisum objective function generated by the SA kernel will yield a vector that, loosely speaking, bisects the sector between the atoms. The EC kernel exhibits very similar behavior but leads to a smoother objective function. As shown in Figure 2, this allows for the determination of a projection vector without ambiguity, even if the atom configuration contains perfect symmetry.

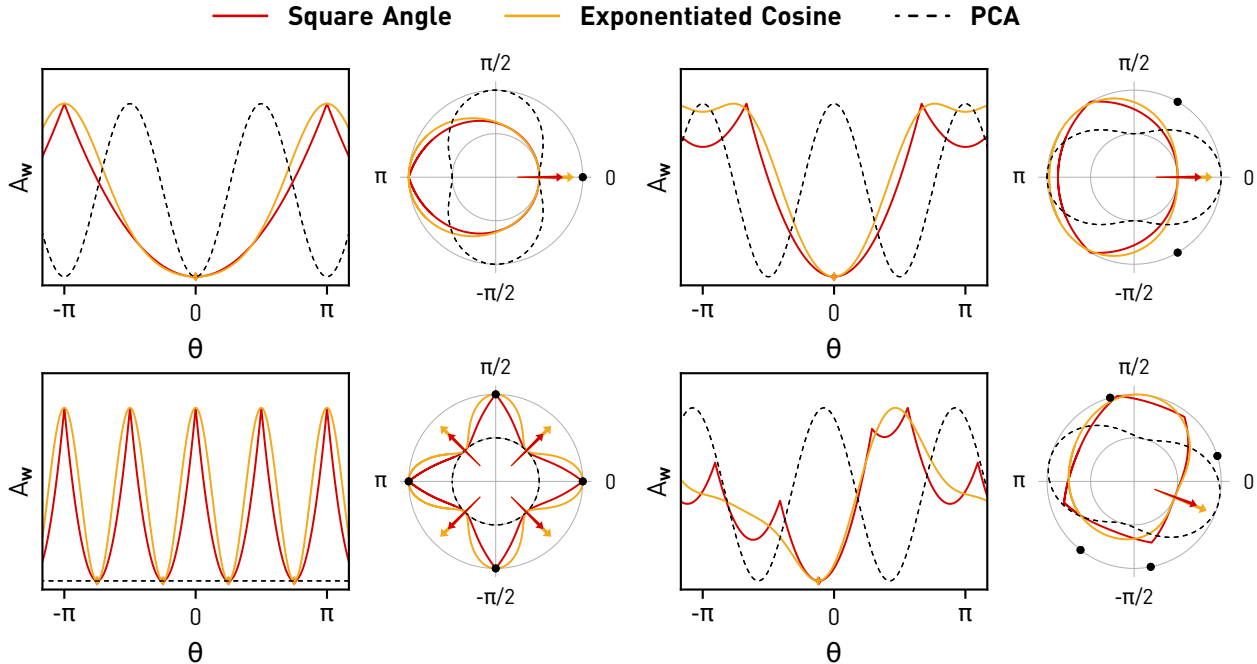


Figure 2: Shown here is an illustration of the minisum algorithm that determines projection vectors for rotational invariant description of atomistic neighbor configurations. Black dots represent atoms which all carry equal importance. The vectors that point from the origin to the atoms are used as the input to bivariate kernels to compute the minisum objective function, which are drawn in solid lines. For reference, the negated values of the PCA objective function are drawn in dashed lines. Projection vectors are obtained by finding the unit vector \mathbf{w}^* that minimizes the objective function.

2.2 Solving the Kernel Minisum Optimization Problems

The optimization problem can be solved very efficiently using a gradient descent algorithm as detailed below.

Square Angle: The objective function of the minisum problem using the square angle (SA) kernel is

$$A_{SA}(\mathbf{w}) \doteq \frac{1}{2} \sum_{i=1}^N g(r_i) \arccos^2(\mathbf{w}^T \mathbf{e}_i). \quad (12)$$

The gradient of A_{SA} with respect to \mathbf{w} is

$$\nabla_{\mathbf{w}} A_{SA} = \sum_{i=1}^N -g(r_i) \frac{\arccos(\mathbf{w}^T \mathbf{e}_i)}{\sqrt{1 - (\mathbf{w}^T \mathbf{e}_i)^2}} \mathbf{e}_i. \quad (13)$$

Note that $\frac{\arccos(\mathbf{w}^T \mathbf{e}_i)}{\sqrt{1 - (\mathbf{w}^T \mathbf{e}_i)^2}}$ is singular when $\mathbf{w} \parallel \mathbf{e}_i$. This can be treated numerically by replacing the removable singularities at $\mathbf{w}^T \mathbf{e}_i = 1$ with the left-limit $\lim_{\mathbf{w}^T \mathbf{e}_i \rightarrow 1^-} \frac{\arccos(\mathbf{w}^T \mathbf{e}_i)}{\sqrt{1 - (\mathbf{w}^T \mathbf{e}_i)^2}} = 1$, while truncating the gradient near the poles at $\mathbf{w}^T \mathbf{e}_i = -1$.

A local minimum can be iteratively searched for with gradient descent while renormalizing \mathbf{w} after each iteration. Moreover, due to the locally quadratic nature of the objective function, we have found that the Barzilai-Borwein algorithm [23] can significantly accelerate the convergence at a minimal cost. The algorithm is presented in Alg. 1.

Algorithm 1 Gradient descent for solving the square angle minisum problem.

```

1: function MINSQUAREANGLE( $\mathbf{E} = [\mathbf{e}_1, \mathbf{e}_2, \dots, \mathbf{e}_N]$ ,  $\mathbf{G} = [g_1, g_2, \dots, g_N]$ ,  $\mathbf{w}_0$ )
2:    $\mathbf{w} \leftarrow \mathbf{w}_0$ 
3:   repeat
4:     Compute gradient  $\nabla_{\mathbf{w}}$  using Eq. 13.
5:     Obtain tangential component of gradient  $\nabla_{\mathbf{w}}^{\perp} \leftarrow (\mathbf{I} - \mathbf{w}\mathbf{w}^T)\nabla_{\mathbf{w}}$ 
6:     if at step 0 then
7:        $\alpha \leftarrow 0.01$  ▷ Small initial step size for bootstrapping
8:     else
9:        $\alpha \leftarrow \frac{(\mathbf{w} - \mathbf{w}_{-1})^T (\nabla_{\mathbf{w}}^{\perp} - \nabla_{\mathbf{w}_{-1}}^{\perp})}{\|\nabla_{\mathbf{w}}^{\perp} - \nabla_{\mathbf{w}_{-1}}^{\perp}\|^2}$  ▷ Adaptive subsequent steps by Barzilai-Borwein
10:    end if
11:    Save  $\mathbf{w}$  as  $\mathbf{w}_{-1}$ ,  $\nabla_{\mathbf{w}}^{\perp}$  as  $\nabla_{\mathbf{w}_{-1}}^{\perp}$ 
12:    Update  $\mathbf{w} \leftarrow \mathbf{w} - \alpha \nabla_{\mathbf{w}}^{\perp}$  and normalize to unit length
13:  until  $\|\mathbf{w} - \mathbf{w}_{-1}\| < \varepsilon$ 
14:  return  $\mathbf{w}$ 
15: end function

```

Exponentiated Cosine: The objective function of the minisum problem using the exponentiated cosine (EC) kernel is:

$$A_{EC}(\mathbf{w}) \doteq \sum_{i=1}^N g(r_i) \exp(-\mathbf{w}^T \mathbf{e}_i). \quad (14)$$

The gradient of A_{EC} with respect to \mathbf{w} is

$$\nabla_{\mathbf{w}} A_{EC} = \sum_{i=1}^N -g(r_i) \exp(-\mathbf{w}^T \mathbf{e}_i) \mathbf{e}_i. \quad (15)$$

The gradient contains no singularity. However, it is not always locally quadratic. This can cause the Barzilai-Borwein algorithm to generate negative step sizes and consequently divert the search towards a local maximum. Luckily, this can be easily overcome by using the absolute value of the step size as calculated by the Barzilai-Borwein algorithm to prevent the minimization algorithm from going uphill. The complete algorithm is given in Alg. 2.

Algorithm 2 Gradient descent for solving the exponentiated cosine minisum problem.

```

1: function MINEXPCOSINE( $\mathbf{E} = [\mathbf{e}_1, \mathbf{e}_2, \dots, \mathbf{e}_N]$ ,  $\mathbf{G} = [g_1, g_2, \dots, g_N]$ ,  $\mathbf{w}_0$  )
2:    $\mathbf{w} \leftarrow \mathbf{w}_0$ 
3:   repeat
4:     Compute gradient  $\nabla_{\mathbf{w}}$  using Eq. 15.
5:     Obtain tangential component of gradient  $\nabla_{\mathbf{w}}^{\perp} \leftarrow (\mathbf{I} - \mathbf{w}\mathbf{w}^T)\nabla_{\mathbf{w}}$ 
6:     if at step 0 then
7:        $\alpha \leftarrow 0.01$  ▷ Small initial step size for bootstrapping
8:     else
9:        $\alpha \leftarrow \left| \frac{(\mathbf{w} - \mathbf{w}_{-1})^T (\nabla_{\mathbf{w}}^{\perp} - \nabla_{\mathbf{w}_{-1}}^{\perp})}{\|\nabla_{\mathbf{w}}^{\perp} - \nabla_{\mathbf{w}_{-1}}^{\perp}\|^2} \right|$  ▷ Adaptive subsequent steps by Barzilai-Borwein
10:    end if
11:    Save  $\mathbf{w}$  as  $\mathbf{w}_{-1}$ ,  $\nabla_{\mathbf{w}}^{\perp}$  as  $\nabla_{\mathbf{w}_{-1}}^{\perp}$ 
12:    Update  $\mathbf{w} \leftarrow \mathbf{w} - \alpha \nabla_{\mathbf{w}}^{\perp}$  and normalize to unit length
13:  until  $\|\mathbf{w} - \mathbf{w}_{-1}\| < \varepsilon$ 
14:  return  $\mathbf{w}$ 
15: end function

```

As shown in Table 2, both Alg. 1 and Alg. 2 converge quickly and consistently handling a wide range of representative point configurations commonly found in molecular systems. However, the gradient descent method can only find local optima. Thus, multiple trials should be performed using different initial guesses to ensure that a global minimum can be located.

2.3 Complete Set of Orthogonal Projection Vectors as A Canonical Coordinate Frame

In 3D, a complete set of orthogonal bases can be found greedily using the protocol as described in Alg. 3. Specifically, we use the globally optimal solution of the minisum optimization problem as the first basis \mathbf{b}_{α} , and the constrained optimal solution in a plane orthogonal to \mathbf{b}_{α} as the second basis \mathbf{b}_{β} . Special care must be taken for determining the third basis \mathbf{b}_{γ} , as the only degree of freedom now is its sign due to the orthogonality constraint. The straightforward approach of choosing the direction that gives the smaller objective function value may fail, for example, when the system contains improper rotational symmetry. In that case, \mathbf{b}_{α} and \mathbf{b}_{β} are interchangeable and both perpendicular to the rotation-reflection axis. As a result, the two candidates of \mathbf{b}_{γ} will both align with the rotation-reflection axis and are thus indistinguishable

Table 2: Listed here is the number of iterations and initial guesses used by the gradient descent algorithm to find an local optimum solution of the kernel minisum problems. The numbers are averaged over 500 repetitions, and the convergence criterion is 10^{-14} . In cases where the iterative algorithm does not converge within 64 iterations, the optimization will be restarted with a new guess.

Kernel	Square Angle		Exponentiated Cosine	
	Itrs./Guess	Guesses	Itrs./Guess	Guesses
Single point	8.8	1	7.9	1
Two point, angle $< \pi/2$	7.1	1	7.7	1
Two point, angle $\geq \pi/2$	6.1	1	6.3	1
Two point, angle $= \pi$	6.0	1	5.6	1
Planar C_3	6.2	1	6.3	1
Planar C_4	5.6	1	6.9	1
Tetrahedra	10.6	1	7.7	1
Octahedra	11.7	1	9.4	1
Improper S_4	17.9	1	23.1	1
Improper S_6	14.7	1	18.0	1
2D random 10 points	7.2	1.1	8.9	1
3D random 50 points	16.9	1.2	14.4	1

by kernel minisum. However, the projection of the atoms into the two seemingly equivalent coordinate frames are not identical, but rather mirror images of each other. Fortunately, this can be addressed by choosing the direction of the half-space, as created by the plane \mathbf{b}_α - \mathbf{b}_β , that yields the smaller kernel objective function between the *bisector* of \mathbf{b}_α and \mathbf{b}_β versus the points lies in that half-space. This rule can also handle general situations with/without symmetry.

Algorithm 3 The procedure for determining a canonical coordinate frame using kernel minisum.

```

1: function GETCANONICALPROJECTION3D( $\mathbf{E} = [\mathbf{e}_1, \mathbf{e}_2, \dots, \mathbf{e}_N]$ ,  $\mathbf{G} = [g_1, g_2, \dots, g_N]$ )
2:    $\mathbf{b}_\alpha \leftarrow$  global minimum of MINISUM( $\mathbf{E}, \mathbf{G}$ ) using multiple runs of Alg. 1 or Alg. 2
3:   if  $\mathbf{E}$  contains only 1 point then
4:     construct arbitrary  $\mathbf{b}_\beta \perp \mathbf{b}_\alpha$ 
5:      $\mathbf{b}_\gamma \leftarrow \mathbf{b}_\alpha \times \mathbf{b}_\beta$ 
6:   else
7:      $\mathbf{b}_\beta \leftarrow$  global minimum of MINISUM( $\mathbf{E}, \mathbf{G}$ ) using multiple runs of Alg. 1 or Alg. 2, subjecting to
       the constraint that the probe vector and the gradient are all  $\perp \mathbf{b}_\alpha$ 
8:      $\mathbf{d} \leftarrow (\mathbf{b}_\alpha + \mathbf{b}_\beta) / \sqrt{2}$ 
9:     if  $\sum \forall \mathbf{e}_i: \mathbf{e}_i^\top (\mathbf{b}_\alpha \times \mathbf{b}_\beta) \geq 0 \quad g_i \kappa(\mathbf{d}, \mathbf{e}_i) \leq \sum \forall \mathbf{e}_i: \mathbf{e}_i^\top (\mathbf{b}_\alpha \times \mathbf{b}_\beta) < 0 \quad g_i \kappa(\mathbf{d}, \mathbf{e}_i)$  then
10:       $\mathbf{b}_\gamma \leftarrow \mathbf{b}_\alpha \times \mathbf{b}_\beta$ 
11:    else
12:       $\mathbf{b}_\gamma \leftarrow -\mathbf{b}_\alpha \times \mathbf{b}_\beta$ 
13:    end if
14:  end if
15:  return  $\mathbf{b}_\alpha, \mathbf{b}_\beta, \mathbf{b}_\gamma$ 
16: end function

```

3 Density-Encoded Canonically Aligned Fingerprint

3.1 Density Field and Approximation of Volume Integral

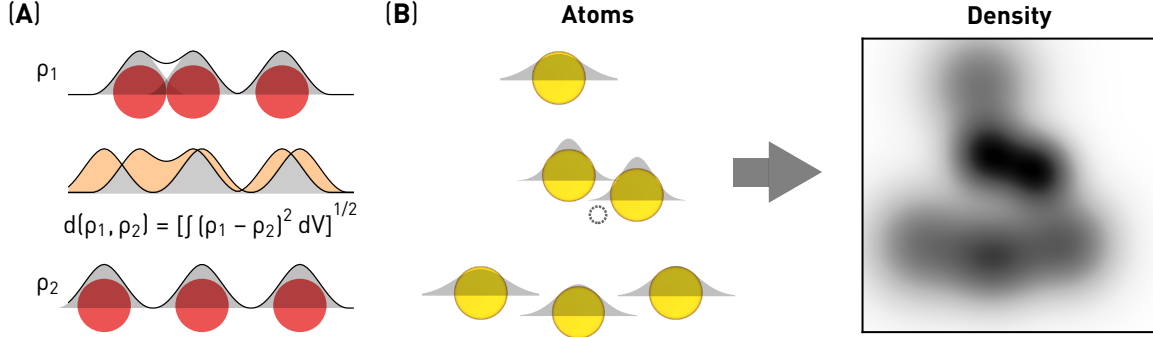


Figure 3: **(A)** Two 1D density profiles, ρ_1 and ρ_2 , are generated from two different atomistic configurations using atom-centered smoothing kernel functions. The ‘distance’ between them is measured as the L_2 norm of their difference, which corresponds to the highlighted area in the middle plot. **(B)** Shown here is a 2D density field using smoothing kernels whose widths depend on the distances of the atoms from the origin. Darker shades indicate higher density.

The local density field $\rho_s(\mathbf{r})$ around a point \mathbf{s} is formulated as a superimposition of smoothing kernel functions each centered at a neighbor atom $i = 1, 2, \dots, N$ with relative displacement \mathbf{x}_i with regard to \mathbf{s} and within a cutoff distance R_c :

$$\rho_s(\mathbf{r}) = \sum_{i, \|\mathbf{x}_i - \mathbf{s}\| < R_c}^N W_c(\mathbf{x}_i - \mathbf{s}) W_d(\mathbf{x}_i, \mathbf{r}) \quad (16)$$

This density field, as has been pointed out previously [12], may be used as a fingerprint of the local atomistic environment. To achieve rotational invariance, we transform the atom coordinates into the canonical coordinate frame $\mathbf{R} \doteq [\mathbf{b}_\alpha, \mathbf{b}_\beta, \mathbf{b}_\gamma]$ as determined by the kernel minisum algorithm:

$$\rho_s(\mathbf{r}) = \sum_{i, \|\mathbf{x}_i - \mathbf{s}\| < R_c}^N W_c(\mathbf{R}^\top \mathbf{x}_i - \mathbf{s}) W_d(\mathbf{R}^\top \mathbf{x}_i, \mathbf{r}). \quad (17)$$

Depending on the specific application, \mathbf{s} may not necessarily overlap with any of the \mathbf{x}_i . Here, we assume that the smoothing kernel W_d takes the form of a stationary Gaussian $\sigma^{-1} \exp[-\|\mathbf{r}\|^2/2\sigma^2]$, but will later discuss about other possibilities in Section 3.2. The density scaling function W_c ensures the continuity of the density field when atoms enter or exit the cutoff distance, and will also be further discussed in a later section. Scalar properties can be acquired directly from the target atom, while vector-valued properties, such as force, can be acquired and interpolated in the local orthogonal coordinates as $\tilde{\mathbf{y}} = \mathbf{R}^\top \mathbf{y}$.

We define the distance between two density fields ρ_i and ρ_j by a weighted L_2 norm of their difference:

$$\Delta\rho_{\mathbf{s}_1\mathbf{s}_2}(\mathbf{r}) \doteq \rho_{\mathbf{s}_1}(\mathbf{r}) - \rho_{\mathbf{s}_2}(\mathbf{r}), \quad (18)$$

$$d(\rho_{\mathbf{s}_1}, \rho_{\mathbf{s}_2}) \doteq \left(\int_{\mathbb{R}^3} w(\mathbf{r}) |\Delta\rho_{\mathbf{s}_1\mathbf{s}_2}(\mathbf{r})|^2 dV(\mathbf{r}) \right)^{1/2}. \quad (19)$$

The weight function $w(\mathbf{r})$ provides additional flexibility for emphasizing particular regions of the atomistic neighborhood, and can strongly facilitate the task of fitting fast varying properties such as the repulsive part of the Lennard-Jones potential.

To efficiently compute the integral, we would like to evaluate the density field using an optimal quadrature rule. To determine the locations and weights of the quadrature nodes, we decompose the volume integral in Eq. 19 into a surface integral over spherical shells and a 1D integral along the radial direction:

$$\int_{\mathbb{R}^3} w(\mathbf{r}) |\Delta\rho_{\mathbf{s}_1\mathbf{s}_2}(\mathbf{r})|^2 dV(\mathbf{r}) = \int_{r=0}^{\infty} \left(\int_{\varphi=0}^{2\pi} \int_{\theta=0}^{\pi} w(r, \theta, \varphi) |\Delta\rho_{\mathbf{s}_1\mathbf{s}_2}(r, \theta, \varphi)|^2 \sin \theta d\theta d\varphi \right) r^2 dr \quad (20)$$

The surface integral can be optimally approximated using the Lebedev quadrature rule [24]:

$$\Delta P_{\mathbf{s}_1\mathbf{s}_2}(r) \doteq \int_{\varphi=0}^{2\pi} \int_{\theta=0}^{\pi} w(r, \theta, \varphi) |\Delta\rho_{\mathbf{s}_1\mathbf{s}_2}(r, \theta, \varphi)|^2 \sin \theta d\theta d\varphi \approx 4\pi \sum_{m=1}^{N_a(r)} w(r, \mathbf{q}_m) \beta_m |\Delta\rho_{\mathbf{s}_1\mathbf{s}_2}(r \cdot \mathbf{q}_m)|^2, \quad (21)$$

where $\beta_m, \mathbf{q}_m \doteq (x_m, y_m, z_m)$, and N_a are the weights, positional unit vectors, and number of the Lebedev nodes, respectively. The radial integral fits well into the generalized Laguerre-Gauss quadrature formula with weight function $r^2 e^{-r}$ [25]:

$$\int_0^{\infty} \Delta P_{\mathbf{s}_1\mathbf{s}_2}(r) r^2 dr \approx \sum_{n=1}^{N_r} \alpha_n e^{r_n} \Delta P_{\mathbf{s}_1\mathbf{s}_2}(r_n), \quad (22)$$

where α_n, r_n , and N_r are the weights, coordinates, and number of the Laguerre nodes, respectively. Combining Eq. 20–22, a composite quadrature rule can be generated consisting of several spherical layers of nodes. As shown in Figure 4, the radial coordinates of the quadrature nodes are determined by the Laguerre quadrature nodes, while the angular positions are determined by the Lebedev quadrature nodes, respectively:

$$\begin{aligned} \int_{\mathbb{R}^3} w(\mathbf{r}) |\Delta\rho_{\mathbf{s}_1\mathbf{s}_2}(\mathbf{r})|^2 dV(\mathbf{r}) &\approx 4\pi \sum_{n=1}^{N_r} \sum_{m=1}^{N_a(n)} \alpha_n \beta_m w_{nm} e^{r_n} |\Delta\rho_{\mathbf{s}_1\mathbf{s}_2}(r_n \cdot \mathbf{q}_m)|^2 \\ &= \sum_{k=1}^N w_k |\rho_i(\mathbf{r}_k) - \rho_j(\mathbf{r}_k)|^2. \end{aligned} \quad (23)$$

Here $k = (n, m); 1 \leq n \leq N_r, 1 \leq m \leq N_a(n)$ is the linearized index of the k -th quadrature node located at $\mathbf{r}_k = r_n \cdot \mathbf{q}_m$ with weight $w_k = 4\pi \alpha_n \beta_m w(r_n \cdot \mathbf{q}_m) e^{r_n}$. A discretized version of Eq. 19 that computes the

distance between the fingerprints is given by:

$$d(\rho_{s_1}, \rho_{s_2}) \approx \left[\sum_{k=1}^N w_k |\rho_{s_1}(\mathbf{r}_k) - \rho_{s_2}(\mathbf{r}_k)|^2 \right]^{1/2}. \quad (24)$$

In addition, the quadrature nodes could be radially scaled such that the outer most nodes lie at a radius R^* within the cutoff distance R_c . This allows us to pair a Laguerre quadrature of any order with an arbitrary cutoff distance. The scaled quadrature rule is given by:

$$\tau = R^* / \max_n(r_n), \quad (25)$$

$$d^*(\rho_{s_1}, \rho_{s_2}) \approx \left[\sum_{k=1}^N \tau^3 w_k |\rho_{s_1}(\tau \mathbf{r}_k) - \rho_{s_2}(\tau \mathbf{r}_k)|^2 \right]^{1/2}. \quad (26)$$

Since the scaling is constant among all nodes, it can be safely omitted in many regression tasks where only the relative difference between the fingerprints are of significance. A list of Laguerre and Lebedev quadrature nodes and weights are given in the Appendix.

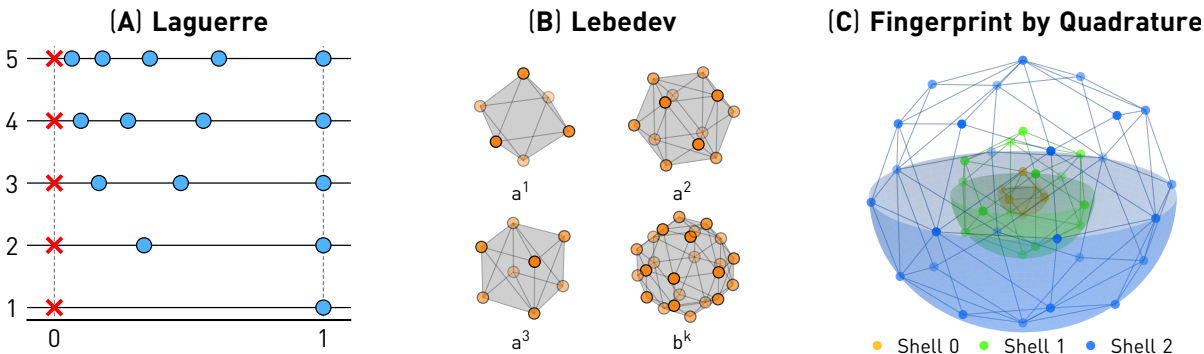


Figure 4: **(A)** Laguerre quadrature nodes with order 1 to 5, normalized by the reciprocal of the largest node onto the unit interval. **(B)** The a^1, a^2, a^3 , and b^k class of Lebedev grid points on a unit sphere. **(C)** The DECAF molecular fingerprint essentially comprises of a grid of quadrature nodes that optimally samples the density field induced by the neighbor atoms. Shown here is an example of one such composite quadrature grid which combines a 3-node Laguerre quadrature rule with three layers of Lebedev quadrature nodes of 3rd, 5th, and 7th order, respectively.

3.2 Radial Weight Functions

In this section, we discuss about two types of weight functions that can be used to fine-tune the density field fingerprint: the density scaling function W_c as in Eq. 17 and the weight of integral $w(r)$ as in Eq. 19.

Driven by the interest of reducing computational cost, we would like to use a cutoff distance to select atoms involved in constructing the density field. However, it is important to ensure that atoms will enter and exit the neighborhood smoothly. This naturally requests that the contribution of an atom to be zero outside of the cutoff, and to increase continuously and smoothly when the atom approaching

entrance. Correspondingly, W_d should: 1) become unity at the origin; 2) smoothly approach zero at the cutoff distance; and 3) be twice-differentiable to ensure the continuity of the fingerprint-based regression. Candidates satisfying the above conditions include, for example, a tent-like kernel

$$W_d(\mathbf{r}) = (1 - \|\mathbf{r}\|/R_c)^t, \quad t > 2 \quad (27)$$

and a bell-shaped polynomial kernel with compact support

$$W_d(\mathbf{r}) = \frac{-b(1 - \|\mathbf{r}\|/R_c)^a + a(1 - \|\mathbf{r}\|/R_c)^b}{a - b}, \quad a > b > 2 \quad (28)$$

as detailed in Appendix.

The approximation of the radial integral using a Laguerre quadrature requires that the integrand, *i.e.* the difference between the atomistic density fields, decays sufficiently fast beyond the outermost quadrature nodes in order to achieve acceptable convergence. In addition, the steeply repulsive yet flat attractive interatomic short-range interactions prompt that the sensitivity of fingerprint be adjusted correspondingly in order to avoid numerical difficulties in training a regression model. The weight of the integral, $w(r)$, provides a convenient means for achieving the purpose. Different from W_d , $w(r)$ should instead satisfy the following conditions: 1) is normalized such that $\int w(r)dV(\mathbf{r}) = 1$; 2) decays sufficiently fast, but not necessarily to 0, beyond the outer most quadrature node; and 3) be sufficiently smooth beyond the outermost quadrature node. Candidates for $w(r)$ includes the tent-like kernel and the bell-shaped kernel for W_d , albeit with a different normalization factor. The Laplacian kernel

$$w(r) = \exp(-|r|/l)/(8\pi l^3), \quad l > 0 \quad (29)$$

with a sufficiently large length scale l also appears to be a candidate due to its similarity with e^{-r} part of the weight function of the Laguerre quadrature. Note that the constant kernel

$$w(r) = 3/(4\pi R_c^3) \quad (30)$$

may also be a choice as long as the density field already decays fast enough due to the density scaling function W_d .

In Figure 5, we demonstrate the effect of the density scaling function and the weight of integral on the distance matrices between fingerprint obtained from a pair of atoms. The comparison between panel A and B shows that a bell-shaped integration weight allows the distance between fingerprints to change more rapidly when the atoms are closer but more slowly when the atoms are farther apart. The visible discontinuity in the second row clearly demonstrates the importance of the damping function when only atoms within a finite cutoff distance are used to compute the fingerprint.

We further examine the impact of the weight functions on the performance of Gaussian process regression (GPR) using the fingerprint of the interatomic force of a minimal system containing two nitrogen atoms. Despite the simplicity of the system, this case is of fundamental importance because of its ubiquity, and because the fast-growing repulsive regime of the Lennard-Jones potential could cause

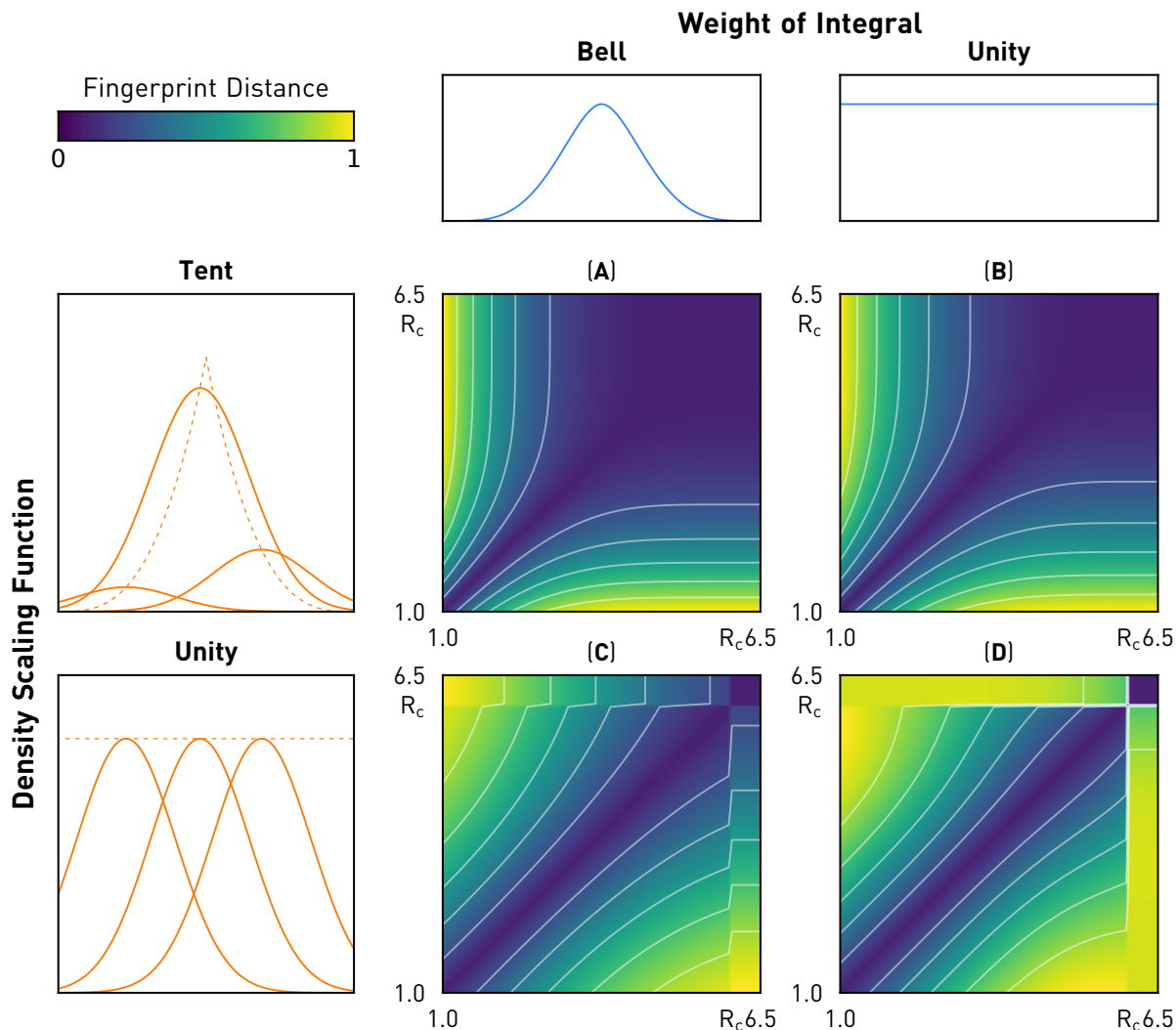


Figure 5: Shown here are examples of the distance matrices between fingerprints sampled from a biatomic system. As manifested by the difference between (A) against (B), a bell-shaped weight of integral helps to emphasize the near field. Meanwhile, the obvious discontinuities in the second row of matrices demonstrate the importance of the density scaling function when the fingerprint algorithm uses only atoms within a finite cutoff distance.

difficulty as a small change in the system configuration can trigger large changes in the regression target function. In Figure 6, we compare the performance among the combination of four weights of the integral and two density scaling functions. The initial training set consists of two samples collected at $r_{N-N} = 1.0$ and 6.0. The regression is then refined using a greedy strategy that consecutively learns the point with the largest posterior variance until the largest uncertainty, defined as twice the posterior standard deviation, is less than 0.1 eV/Å. Thanks to the active learning scheme, all combinations of the weight functions are able to deliver a good fit of the target function after refinement. However, the number of points required and the achieved accuracy vary. Therefore, it is important to evaluate and choose the weight functions in the context of specific application scenarios.

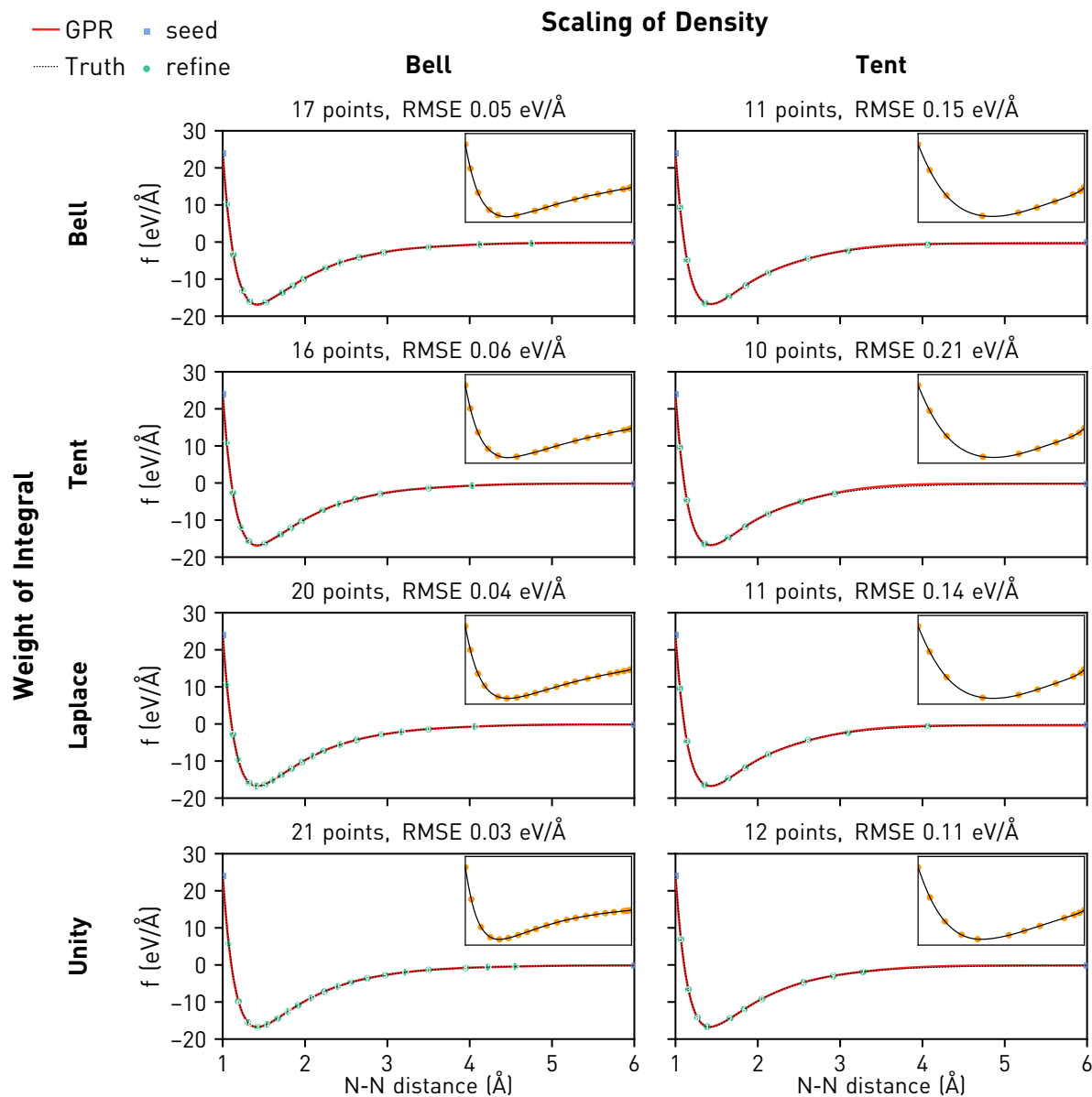


Figure 6: Gaussian process regression of the force between two nitrogen atoms as a function of interatomic distance using different combinations of radial weight functions. Inset figures are plots of the regression function using distances from the feature space.

3.3 Quadrature Resolution

Despite the formal convergence of the composite quadrature in DECAF, a cost of $O(NM)$ distance calculations and kernel evaluations are needed to sample a density field generated by N atoms using M quadrature nodes.¹ Thus, in practice it is often desirable to use as few nodes as possible to capture only information of the density field within a certain band limit [26]. Accordingly, the integral cutoff R_c , the number of quadrature nodes, and the width of the density kernel need to be tuned to obtain an optimal balance between resolution and computational speed.

When designing the composite quadrature rule, we chose the Laguerre quadrature for the radial direction because its nodes are denser near the origin but sparser farther away. This is consistent with our physical intuition that the near field generally has a stronger influence than the far field in an atomistic neighborhood. For example, the Van de Waals potential grows rapidly when atoms are in direct contact, but flattens out of the first coordinate shell. Accordingly, it may be possible for us to use sparser outer-layer grids to reduce the total number of quadrature nodes, while still keeping enough nodes in the inner layers to maintain the sensitivity of the quadrature toward close neighbors. Cooperatively, we can also use non-stationary Gaussian density kernels whose width dependent on the distance from the atom to the origin. In this way, the sparser nodes should still sufficiently sample the smoother far field. Wider kernels at remote atoms also reduce the possible difference between the far fields of two fingerprints. Thus, the contribution of the far field in the integral can be effectively tuned even though the weights on the quadrature nodes remain the same.

In Figure 7, we demonstrate how a variable-resolution quadrature can be combined with a widening smoothing density kernel to simultaneously reduce the computational complexity and preserve the quality of the fingerprint. In column A, a dense grid is used to sample density fields generated by a wide smoothing length. By examining the distance matrices of fingerprints sampled during bond stretching and angular stretching movements, we note that the radial similarity decreases monotonically while the angular similarity changes nearly constantly. In column B, the number of quadrature nodes is kept the same, but the smoothing length is reduced as an attempt to increase fingerprint sensitivity. Better response in the near field of the radial direction is obtained, but the linearity in the far field in the angular direction is compromised. In column C, the fingerprint performs even worse due to the combination of a sparser quadrature grid and a small smoothing length. In column D, the performance recovered because we let the smoothing length depend on the radial distance and adjust the quadrature nodes according to this pattern.

4 Demonstration

4.1 Potential Energy Surface

First, we attempt to fit the potential energy surface of a protonated water dimer system, in a head-to-head configuration, as a function of the oxygen-oxygen distance r_{O-O} and the dihedral angle φ between the

¹A L^2 distance calculation using the extracted feature vectors comes at a cost of $O(M)$ floating point operations.

two planes each formed by a water molecule. As shown in Figure 8A, the system contains an improperly rotational symmetry, which we wish to capture with the kernel minisum algorithm. A GPR model was seeded with 8 training points corresponding to the combinations of $r_{\text{O-O}} = 2.2, 2.4, 2.6, 2.8$ and $\varphi = 0, \pi/2$. Subsequently, an active learning protocol was used to greedily absorb points with the highest uncertainty into the training set. Despite that we restricted all training data to be within the subdomain $\varphi \leq \pi/2$, as shown by Figure 8B and 8C, we are able to accurately reproduce the target function over the entire parameter space after a few active learning steps.

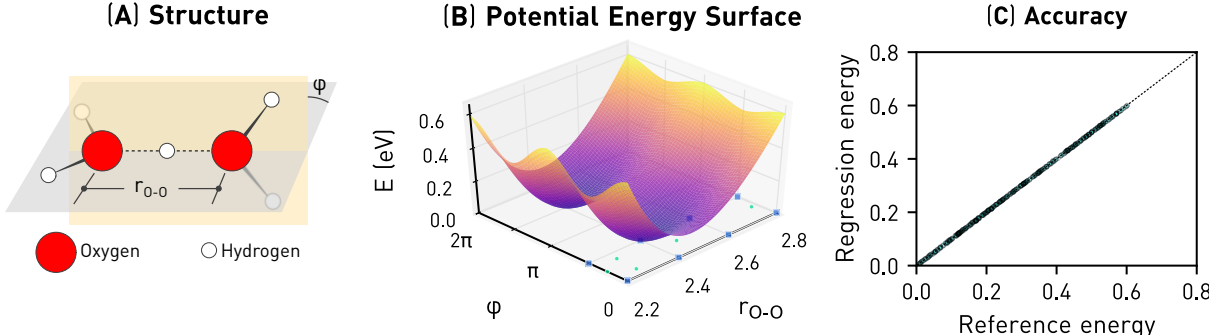


Figure 8: Gaussian process regression is carried out to fit the potential energy surface of a protonated water dimer as a function of two internal variables, *i.e.* the oxygen-oxygen distance $r_{\text{O-O}}$ and the dihedral angle φ between the plane determined by the two water molecules. This system contains an improperly rotational symmetry, which can be correctly recognized by the kernel minisum-based algorithm given in Alg. 3. Only a quarter of the domain was used to train the GP, yet the model can accurately predict the energy of the entire parameter space thanks to symmetry detection.

4.2 Geometry Optimization and Vibrational Analysis

Next, we demonstrate the usability of fingerprint for fitting vector-valued quantities by performing geometry optimization and vibrational analysis on a single water molecule. The process involves the simultaneous regression of: 1) energy, a molecular scalar quantity; 2) force, a per-atom vector quantity; and 3) dipole, a molecular vector quantity. Correspondingly, we performed GPR of energy and dipole using fingerprints extracted from the center of mass of the molecule, and GPR of force using fingerprints extracted from each atom. The training set consists of 45 configurations uniformly covering the range $r_{\text{O-H}} = 0.93, 0.95, 0.97, 0.99, 1.05 \text{ \AA}$ and $\theta_{\text{H-O-H}} = 101^\circ, 105.5^\circ, 111^\circ$. As shown in Table 3, the GPR model can successfully drive calculations of the infrared spectrum of the molecule from randomly perturbed initial structures in arbitrary orientation.

5 Discussion

5.1 Canonical Coordinate Frame

A major advantage of our kernel minisum approach as compared to PCA using the L^p norm, lies in its 1) robustness in the presence of structural symmetry; and 2) continuity of the resulting principal axes with

Table 3: Geometry optimization and vibrational analysis of a single water molecule using GPR and our proposed fingerprint algorithm. 256 independent trials were performed using coordinates of water perturbed from equilibrium by a Gaussian noise $\mathcal{N}(\mathbf{0}, 0.15\mathbf{I})$ followed by a randomly chosen rigid-body rotation.

		GPR	DFT	
Zero-point energy		0.591 ± 0.003 eV	0.583 eV	
Static dipole		2.1580 ± 0.0001 D	2.159 D	
Residual Force		0.0016 ± 0.0005 eV/Å	0.0003 eV/Å	
Mode	Frequency (cm ⁻¹)		Intensity (D/Å) ² amu ⁻¹	
	GPR	DFT	GPR	DFT
0	1576.5 ± 1.4	1602.4	1.5726 ± 0.0005	1.5767
1	3819.3 ± 0.9	3817.5	0.2516 ± 0.0005	0.2159
2	3916.7 ± 1.6	3922.6	1.3349 ± 0.0028	1.3401

respect to angular movement of the input data. As shown in Figure 9, kernel minisum is particularly suitable for atomistic systems where strong symmetries are common and the continuity against angular movement is desired. The minisum framework can also be used with other customized kernels to suit for the characteristics of specific application scenarios.

5.2 Connection to Other Fingerprint Algorithms

In Figure 10, we compare the ability to distinguish atomistic configurations of our fingerprint as well as SOAP and the Coulomb matrix. Our work is inspired by the SOAP descriptor [12], which proposes the use of smoothed densities to represent atomistic neighborhoods. However, instead of converting the density field into the frequency domain using spherical harmonics, we perform density field sampling and comparison directly in the real space. This is enabled thanks to the available of canonical coordinate frame as computed through the kernel minisum optimization. We have mainly used the L_2 norm to compute the distance between atomistic neighborhoods. However, our fingerprint exhibits very similar behavior to SOAP when used together with an inner product formula

$$d(\rho_{\mathbf{s}_1}, \rho_{\mathbf{s}_2}) \approx \frac{\sum_{k=1}^N w_k \rho_{\mathbf{s}_1}(\mathbf{r}_k) \rho_{\mathbf{s}_2}(\mathbf{r}_k)}{\sqrt{\sum_{k=1}^N w_k \rho_{\mathbf{s}_1}(\mathbf{r}_k) \rho_{\mathbf{s}_1}(\mathbf{r}_k)} \sqrt{\sum_{k=1}^N w_k \rho_{\mathbf{s}_2}(\mathbf{r}_k) \rho_{\mathbf{s}_2}(\mathbf{r}_k)}} \quad (31)$$

as demonstrated in Figure 10A. Thus, our fingerprint could be used in conjunction with a wide variety of covariance functions based on either the Euclidean distance or the inner product similarity.

At first sight, DECAF is very different from the Coulomb matrix fingerprint and GRAPE, which are both graph-based algorithms [17, 18]. However, instead of trying to capture the overall density field, if we measure the contribution from each individual atom on the quadrature nodes at $\mathbf{z}_1, \mathbf{z}_2, \dots, \mathbf{z}_M$ as a row

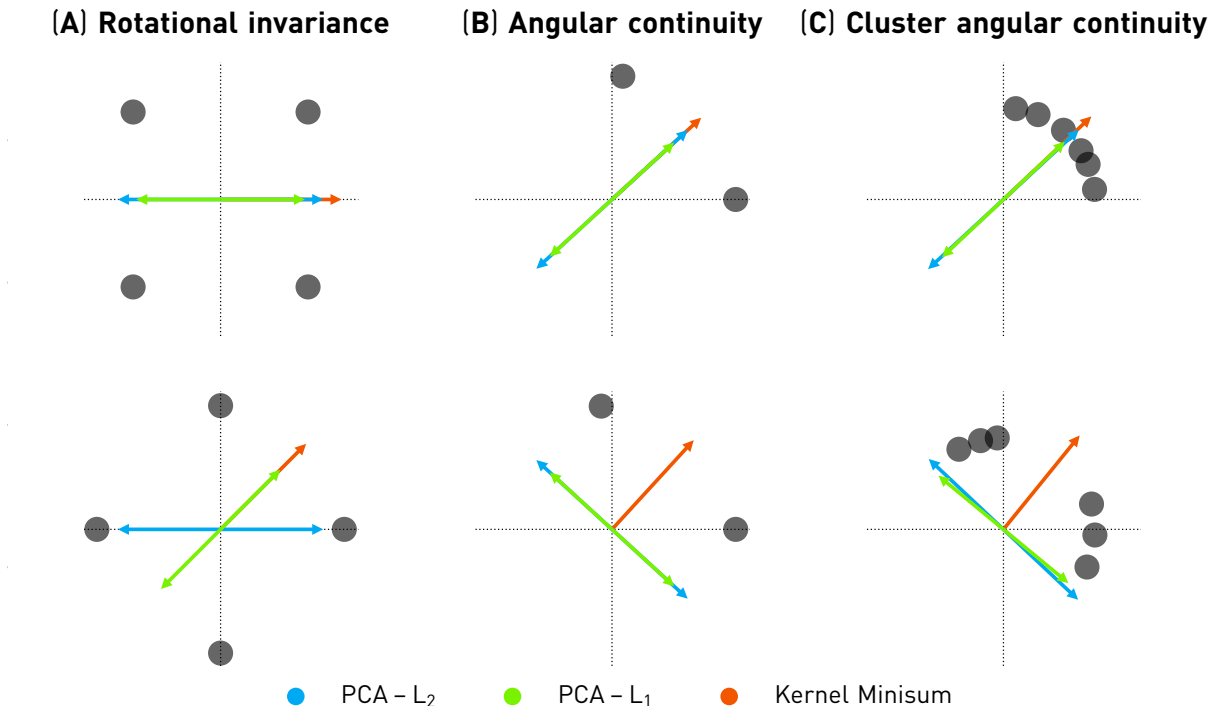


Figure 9: A comparison of the orthogonal bases obtained using principal components analysis (PCA) and kernel minisum with the square-angle (MSA) kernel. **(A)** The PCA algorithm, used in conjunction with the L_2 norm, fails to extract a principal axis that rotates with a system that exhibits planar C_4 symmetry. Both MSA and PCA with the L_1 norm can accommodate this scenario. **(B)** Both L_1 and L_2 principal axes change orientation abruptly when the system undergoes a slight angular motion. In contrast, the MSA output is continuous with regard to this movement as it always bisects the angle formed by the atoms and the origin. **(C)** Loosely speaking, the MSA axis points at the majority direction of the atoms if only a single cluster is present within the cutoff distance, but bisects the angle between two atom clusters. This is different from PCA-based results and should deliver robust rotational invariance as well as continuity. Arrows are drawn at different lengths to improve visual clarity in situations of overlapping. They are to be understood as unit vectors. De-trending is not performed because the radial distances of the atoms carry physically significant information.

vector, and stacked up the results to yield the matrix

$$\mathbf{E}_{ij}^{N \times M} = k(\mathbf{x}_i, \mathbf{z}_j). \quad (32)$$

Then \mathbf{E} can be regarded as an incidence matrix [27] between atoms and the quadrature nodes. This is similar to the graph-based abstraction as seen in the Coulomb matrix and the GRAPE kernel. However, in both cases the vertices in the graph represent atoms while the edges represent pairwise interatomic interactions. Here, the density-based incidence matrix adopts the opposite pattern and constructs a graph with the quadrature nodes being vertices and atoms being edges. The adjacency matrix in this case is

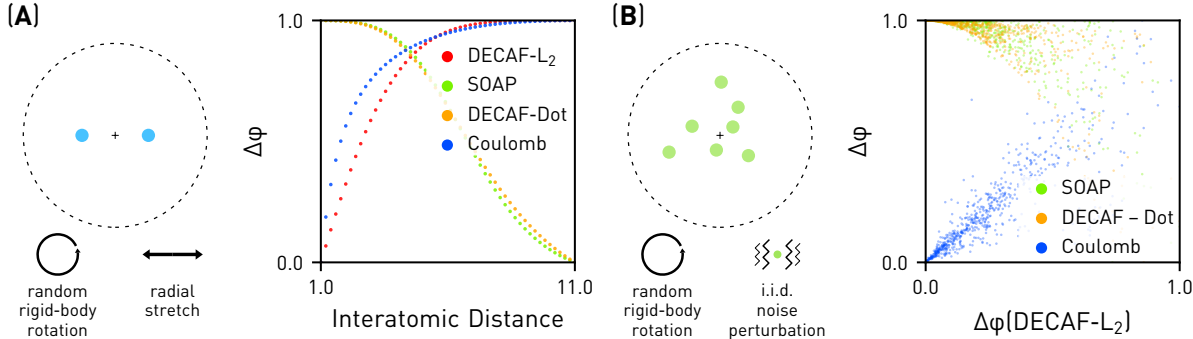


Figure 10: A comparison between the distance measure used DECAF, SOAP, and the Coulomb matrix. Fingerprint distances $\Delta\phi$ shown in the plots are measured against $r_{ij} = 1.0$ in (A) and an randomly chosen initial state in (B).

computed as the inner product $\mathbf{E}^\top \mathbf{E}$:

$$\mathbf{A}_{ij}^{M \times M} = (\mathbf{E}^\top \mathbf{E})_{ij} = \sum_{k=1}^N k(\mathbf{x}_k, \mathbf{z}_i) k(\mathbf{x}_k, \mathbf{z}_j). \quad (33)$$

The weight on the edges, as represented by the elements of the adjacency matrix A , can be interpreted as the total flux as contributed by all paths each bridged by an atom k . We have numerically found that the smallest N eigenvalues (except for the 0 eigenvalue) of the symmetric normalized Laplacian

$$\mathbf{L} = \mathbf{I} - \mathbf{D}^{-1/2} \mathbf{A} \mathbf{D}^{-1/2}, \text{ where } \mathbf{D}_{ii} = \delta_{ij} \sum_j \mathbf{A}_{ij} \quad (34)$$

is invariant under rotation up to a certain noise level, even if the quadrature nodes do not rotate with the atoms. Nonetheless, this detour appears to represent a pure theoretical interest rather than any practical value.

6 Conclusion

In this paper, we presented the Density-Encoded Canonically Aligned Fingerprint (DECAF) by exploring the idea of using smoothed density fields to represent and compare atomistic neighborhoods. One of the key enabling technique in DECAF is a kernel minisum algorithm, which allows the unambiguous identification of a canonically aligned coordinate frame that can be used for rotationally invariant projection of the density field as well as any associated vector quantities. We have performed detailed analysis to study the behavior of the fingerprint by changing various parameter, such as resolution, smoothing length, and the choice of weight functions. We demonstrate that the fingerprint algorithm can be used to implement highly accurate regressions of both scalar and vector properties of atomistic systems including energy, force and dipole moment, and could be a useful building block for constructing data-driven next generation force fields for various applications such as molecular dynamics simulations and molecular

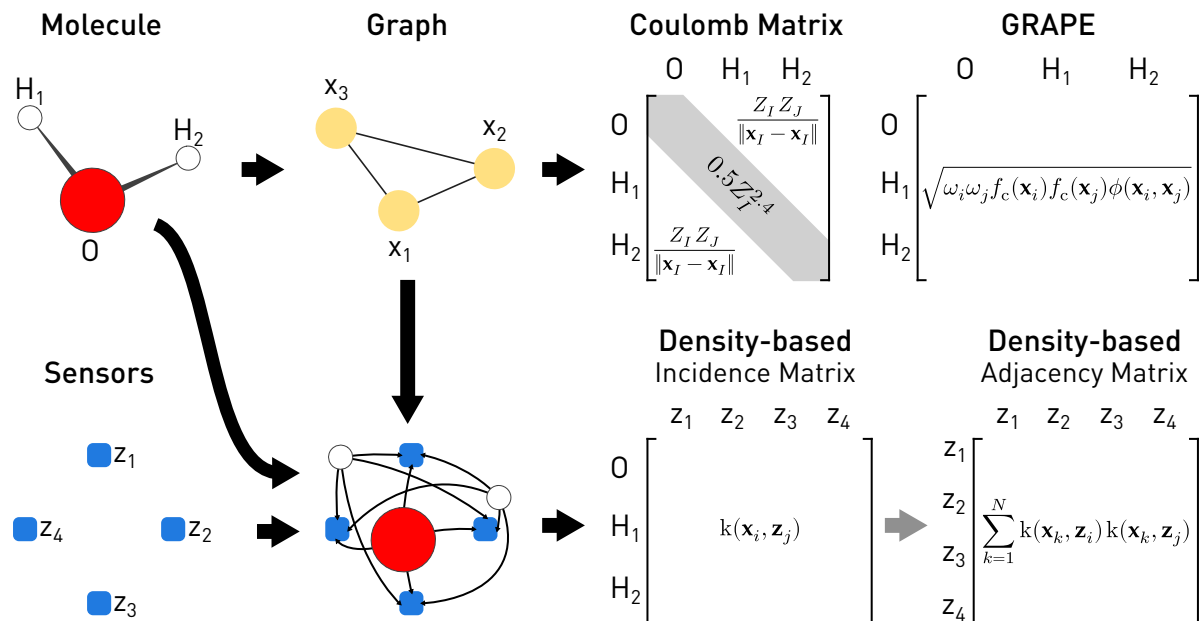


Figure 11: A comparison between graph-based molecular fingerprints. The Coulomb Matrix and the GRAPE kernel construct graphs where nodes corresponds to atoms while the weights on the edges are determined by some pairwise inter-atomic interactions. In contrast, in the density-based incidence matrix we construct a graph on a set of quadrature nodes whose connectivity is weighted by a sum of contributions from individual atoms.

docking.

Acknowledgment

This work was supported by the Department of Energy (DOE) Collaboratory on Mathematics for Mesoscopic Modeling of Materials (CM4). This work was also supported by the Army Research Laboratory under Cooperative Agreement Number W911NF-12-2-0023.

References

- [1] G. Zhao, J. R. Perilla, E. L. Yufenyuy, X. Meng, B. Chen, J. Ning, J. Ahn, A. M. Gronenborn, K. Schulten, C. Aiken, and Others. Mature HIV-1 capsid structure by cryo-electron microscopy and all-atom molecular dynamics. *Nature*, 497(7451):643–646, 2013.
- [2] K. Lindorff-Larsen, P. Maragakis, S. Piana, and D. E. Shaw. Picosecond to Millisecond Structural Dynamics in Human Ubiquitin. *The Journal of Physical Chemistry B*, 120(33):8313–8320, 2016.
- [3] A. K. Rappe, C. J. Casewit, K. S. Colwell, W. A. Goddard, and W. M. Skiff. UFF, a full periodic table force field for molecular mechanics and molecular dynamics simulations. *Journal of the American Chemical Society*, 114(25):10024–10035, 1992.

- [4] W. D. Cornell, P. Cieplak, C. I. Bayly, I. R. Gould, K. M. Merz, D. M. Ferguson, D. C. Spellmeyer, T. Fox, J. W. Caldwell, and P. A. Kollman. A second generation force field for the simulation of proteins, nucleic acids, and organic molecules. *Journal of the American Chemical Society*, 117(19):5179–5197, 1995.
- [5] W. L. Jorgensen, D. S. Maxwell, and J. Tirado-Rives. Development and Testing of the OPLS All-Atom Force Field on Conformational Energetics and Properties of Organic Liquids. *Journal of the American Chemical Society*, 118(15):11225–11236, 1996.
- [6] D. Frenkel and B. Smit. *Understanding molecular simulation: from algorithms to applications*, volume 1. Academic press, 2001.
- [7] A. R. Leach. *Molecular modelling: principles and applications*. Pearson education, 2001.
- [8] T. Cheng, A. Jaramillo-Botero, W. A. Goddard, and H. Sun. Adaptive accelerated ReaxFF reactive dynamics with validation from simulating hydrogen combustion. *Journal of the American Chemical Society*, 136(26):9434–9442, 2014.
- [9] D. Braun, S. Boresch, and O. Steinhauser. Transport and dielectric properties of water and the influence of coarse-graining: Comparing BMW, SPC/E, and TIP3P models. *The Journal of Chemical Physics*, 140(6):064107, 2014.
- [10] S. Boonstra, P. R. Onck, and E. van der Giessen. CHARMM TIP3P Water Model Suppresses Peptide Folding by Solvating the Unfolded State. *The Journal of Physical Chemistry B*, 120(15):3692–3698, 2016.
- [11] J. Behler. Atom-centered symmetry functions for constructing high-dimensional neural network potentials. *The Journal of Chemical Physics*, 134(134), 2011.
- [12] A. P. Bartók, R. Kondor, and G. Csányi. On representing chemical environments. *Physical Review B*, 87(18):184115, 2013.
- [13] Z. Li, J. R. Kermode, and A. De Vita. Molecular Dynamics with On-the-Fly Machine Learning of Quantum-Mechanical Forces. *Physical Review Letters*, 114(9):096405, 2015.
- [14] A. Khorshidi and A. A. Peterson. Amp: A modular approach to machine learning in atomistic simulations. *Computer Physics Communications*, 207:310–324, 2016.
- [15] C. E. Rasmussen and C. K. I. Williams. *Gaussian Processes for Machine Learning*. 2006.
- [16] D. Specht. A general regression neural network. *IEEE Transactions on Neural Networks*, 2(6):568–576, 1991.
- [17] M. Rupp, A. Tkatchenko, K.-R. Müller, O. A. von Lilienfeld, K.-R. R. Müller, O. Anatole Von Lilienfeld, and O. A. von Lilienfeld. Fast and accurate modeling of molecular atomization energies with machine learning. *Physical Review Letters*, 108(5):58301, 2012.
- [18] G. Ferré, T. Haut, and K. Barros. Learning molecular energies using localized graph kernels. *The Journal of Chemical Physics*, 146(11):114107, 2017.

- [19] H. Y. Sun. *Learning over Molecules : Representations and Kernels*. PhD thesis, Harvard University, 2014.
- [20] R. R. Coifman, S. Lafon, A. B. Lee, M. Maggioni, B. Nadler, F. Warner, and S. W. Zucker. Geometric diffusions as a tool for harmonic analysis and structure definition of data: diffusion maps. *Proceedings of the National Academy of Sciences of the United States of America*, 102(21):7426–31, 2005.
- [21] A. P. Bartók, M. C. Payne, R. Kondor, and G. Csányi. Gaussian Approximation Potentials: The Accuracy of Quantum Mechanics, without the Electrons. *Physical Review Letters*, 104(13):136403, 2010.
- [22] V. Botu and R. Ramprasad. Learning scheme to predict atomic forces and accelerate materials simulations. *Physical Review B*, 92(9):094306, 2015.
- [23] J. BARZILAI and J. M. BORWEIN. Two-Point Step Size Gradient Methods. *IMA Journal of Numerical Analysis*, 8(1):141–148, 1988.
- [24] D. Lebedev, VI and Laikov. A quadrature formula for the sphere of the 131st algebraic order of accuracy. *Doklady. Mathematics*, 59(3):477–481, 1999.
- [25] P. Rabinowitz and G. Weiss. Tables of Abscissas and Weights for Numerical Evaluation of Integrals of the Form $\int_0^\infty e^{-x} x^n f(x) dx$. *Mathematical Tables and Other Aids to Computation*, 13(68):285–294, 1959.
- [26] B. Leistedt and J. D. McEwen. Exact Wavelets on the Ball. *IEEE Transactions on Signal Processing*, 60(12):6257–6269, 2012.
- [27] J. L. Gross and J. Yellen. *Graph theory and its applications*. Chapman & Hall/CRC, 2005.
- [28] M. Liu, G. Liu, and K. Lam. Constructing smoothing functions in smoothed particle hydrodynamics with applications. *Journal of Computational and Applied Mathematics*, 155(2):263–284, 2003.
- [29] L. B. Lucy. A numerical approach to the testing of the fission hypothesis. *The Astronomical Journal*, 82(12), 1977.

Appendix

Polynomial Smoothing Functions with Compact Support

As candidates for the weight of integral and density scaling functions (Section 3.2), a class of compact polynomials that satisfy the criteria [28]:

1. is compactly supported,
2. is strictly positive within some cutoff distance r_c ,
3. decreases monotonically,
4. is at least twice continuously differentiable

with minimal number of non-zero terms are:

$$W^{a,b}(s) = \frac{-bs^a + as^b}{\sigma}, \quad a > b > 2, \quad (35)$$

where $s = 1 - r/h$ is the normalized complementary coordinate within the span h of the kernel, and

$$\sigma = 8\pi h^3 \left(\frac{a}{b^3 + 6b^2 + 11b + 6} - \frac{b}{a^3 + 6a^2 + 11a + 6} \right) \quad (36)$$

is an optional normalization factor to ensure that the integral of the kernel in a 3D ball of radius h is unity. The parameters a and b are free parameters that can be used to adjust the smoothness and width of the kernel, and can take any real numbers satisfying the condition $a > b > 2$. Note that the kernel $W^{4,3}$ is equivalent to the Lucy kernel commonly used in Smoothed Particle Hydrodynamics simulations [29]. The kernel can be evaluated very efficiently using only multiplication and addition when both a and b are integers.

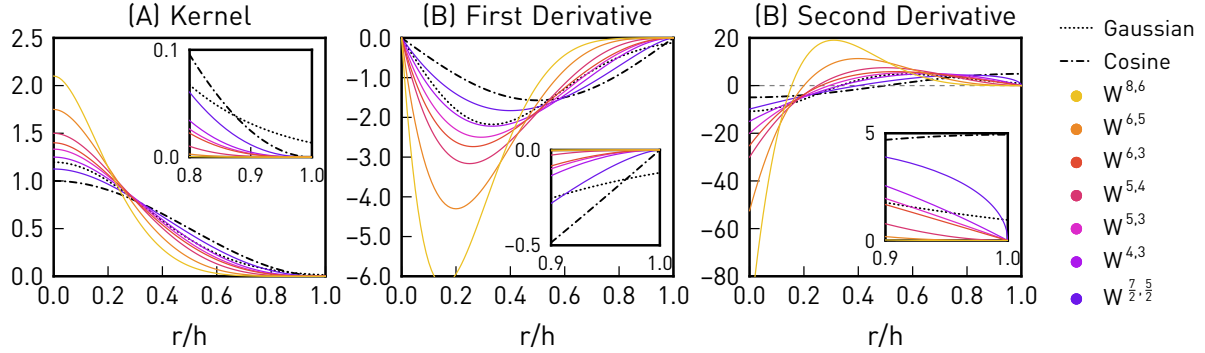


Figure 12: Visualization of the polynomial kernels as given in Eq. 35 with a unit support radius. The kernels are bell-shaped with a derivative of 0 at the origin. Both the first and second derivatives of the kernels transition smoothly to 0 at its support radius. In contrast, the Gaussian kernel and its derivatives does not decay to zero at any finite distance, while the second derivative of the Cosine kernel as mentioned in previous work [11, 12] is not zero at the cutoff distance.

Table of Quadrature Nodes and Weights

In the table below, we list the nodes and weights of the Laguerre quadrature rules up to $N_r = 6$, using notations from Eq. 22.

		n = 0	n = 1	n = 2	n = 3	n = 4	n = 5
Nr = 2	r_n	2.00000	6.00000				
	a_n	1.50000	0.50000				
Nr = 3	r_n	1.5174	4.3116	9.1710			
	a_n	1.0375	0.9058	0.0568			

Nr = 4	r_n	1.2268	3.4125	6.9027	12.4580		
	a_n	0.7255	1.0634	0.2067	0.0044		

Nr = 5	r_n	1.0311	2.8372	5.6203	9.6829	15.8285	
	a_n	0.5209	1.0667	0.3835	0.0286	0.0003	

Nr = 6	r_n	0.8899	2.4331	4.7662	8.0483	12.6004	19.2620
	a_n	0.3844	0.9971	0.5361	0.0795	0.0029	0.0000
=====							

In the table below, we list the nodes and weights of the Lebedev quadrature rules up to $N_r = 6$, using notations from Eq. 21.

=====				
Na = 6	x_m	y_m	z_m	b_m
m = 0,1	+ -1.000000	0.000000	0.000000	0.16667
m = 2,3	0.000000	+ -1.000000	0.000000	0.16667
m = 4,5	0.000000	0.000000	+ -1.000000	0.16667

Na = 14	x_m	y_m	z_m	b_m
m = 0,1	+ -1.000000	0.000000	0.000000	0.06667
m = 2,3	0.000000	+ -1.000000	0.000000	0.06667
m = 4,5	0.000000	0.000000	+ -1.000000	0.06667
m = 6-13	+ -0.57735	+ -0.57735	+ -0.57735	0.07500

Na = 26	x_m	y_m	z_m	b_m
m = 0,1	+ -1.000000	0.000000	0.000000	0.04762
m = 2,3	0.000000	+ -1.000000	0.000000	0.04762
m = 4,5	0.000000	0.000000	+ -1.000000	0.04762
m = 6-9	0.000000	+ -0.70711	+ -0.70711	0.03810
m = 10-13	+ -0.70711	0.000000	+ -0.70711	0.03810
m = 14-17	+ -0.70711	+ -0.70711	0.000000	0.03810
m = 18-25	+ -0.57735	+ -0.57735	+ -0.57735	0.03214

Na = 38	x_m	y_m	z_m	b_m
m = 0,1	+ -1.000000	0.000000	0.000000	0.00952
m = 2,3	0.000000	+ -1.000000	0.000000	0.00952
m = 4,5	0.000000	0.000000	+ -1.000000	0.00952
m = 6-13	+ -0.57735	+ -0.57735	+ -0.57735	0.03214
m = 14-17	+ -0.45970	+ -0.88807	0.000000	0.02857
m = 18-21	+ -0.88807	+ -0.45970	0.000000	0.02857
m = 22-25	+ -0.45970	0.000000	+ -0.88807	0.02857
m = 26-29	+ -0.88807	0.000000	+ -0.45970	0.02857
m = 30-33	0.000000	+ -0.45970	+ -0.88807	0.02857
m = 34-37	0.000000	+ -0.88807	+ -0.45970	0.02857

Na = 50	x_m	y_m	z_m	b_m
m = 0,1	+ -1.000000	0.000000	0.000000	0.01270
m = 2,3	0.000000	+ -1.000000	0.000000	0.01270
m = 4,5	0.000000	0.000000	+ -1.000000	0.01270

m = 6-9	0.000000	+ - 0.70711	+ - 0.70711	0.02257
m = 10-13	+ - 0.70711	0.000000	+ - 0.70711	0.02257
m = 14-17	+ - 0.70711	+ - 0.70711	0.000000	0.02257
m = 18-25	+ - 0.57735	+ - 0.57735	+ - 0.57735	0.02109
m = 26-33	+ - 0.30151	+ - 0.30151	+ - 0.90453	0.02017
m = 34-41	+ - 0.30151	+ - 0.90453	+ - 0.30151	0.02017
m = 42-49	+ - 0.90453	+ - 0.30151	+ - 0.30151	0.02017
=====				

The Laguerre and Lebedev quadrature nodes can be combined using Eq. 23-26 into composite grids for sampling the atomistic density field.